Properties of phase-coherent energy shuttling on the nanoscale

Roi Baer[a),b)]
Department of Physical Chemistry and the Lise Meitner and Fritz Haber Centers, The Hebrew University of Jerusalem, Jerusalem 91904, Israel

Kenneth Lopata and Daniel Neuhauser[a),c)]
Department of Chemistry and Biochemistry, University of California, Los Angeles, California 90095

Recently, the possibility of transporting electromagnetic energy as local-plasmon-polariton waves along arrays of silver nanoparticles was demonstrated experimentally [S. A. Maier *et al.*, Nat. Mater. **2**, 229 (2003)]. It was shown that dipole coupling facilitates phase-coherent excitation waves, which propagate while competing against decoherence effects occurring within each dot. In this article the authors study the ideal coherent shuttling in such a system, leaving decoherence for future investigation. In the weak field limit, the waves obey a Schrödinger equation, to be solved using either time-dependent wave-packet or energy resolved scattering techniques. The authors study some dynamical characteristics of these waves, emphasizing intuition and insight. Scattering from barriers, longitudinal-transverse coupling and acceleration methods are studied in detail. The authors also discuss briefly two-dimensional arrays and a simple decoherence model. © *2007 American Institute of Physics.* [DOI: 10.1063/1.2390697]

INTRODUCTION

[1][2][3]The interface between optics and electronics is an important subject under extensive study because of the impressive progress in solid-state crystal photonic devices.[1–3] Miniaturization to the nanoscale has been demonstrated using linear arrays of silver nanoparticles for transporting near-field electromagnetic (EM) energy.[4–7] Important advances were made also on the molecular scale, outlining a possible route to functional molecular photonic devices.[8–10] The EM interaction between the active centers (whether particles or molecules) enabling such transport is the resonance dipole coupling.[11–17] We will concentrate in this article particularly on the nanoparticle array. At each site along the array, the EM energy can be stored as a localized surface plasmon (LSP) excitation. The dipole coupling enables the excitation energy to "hop" between different sites, thus forming the localized surface plasmon-polariton (LSPP) waves. Various controllable parameters affect the energy flow, for example, the distance between the nanoparticles, their surrounding dielectric constant, and their shape and composition (for example, core-shell techniques allow us to change significantly the LSP frequency[18–21]). This large set of controllable properties may be valuable for constructing novel LSPP nanoscale devices. These may be important new scientific techniques with obvious technological results, related to the ability to drive EM energy into well-controlled and confined regions.[22–26]

A high-level approach to plasmon-polariton dynamics includes an explicit treatment of the electromagnetic field dynamics by means of a full numerical solution of Maxwell's equations.[27–31] Ideally, this should couple to the material dynamics (electronic and nuclear) within the metallic nanodots. Yet, the resulting theory is complicated (even though efficient methods exist to describe electron dynamics, such as time-dependent density functional theory[32,33]). Instead, simplified models can often capture the essential physical content of the systems.

This article takes a less involved route, which forms a simplified treatment, on the one hand, yet is general enough to capture, in the weak field and large separation limit, most of the important transport properties. This treatment allows us to study plasmon-polariton waveguides, stressing in particular the couplings between polarization modes. The resulting method, relying on quantum scattering theory, is efficient and robust. We also try to develop a qualitative understanding of the dynamics of these waves. The rest of the article includes section on theory, where the model and numerical time-dependent and time-independent methods of solution are given; a section on devices for coherent plasmonics; and a section summary and discussion.

THEORY

Many aspects of the LSPP optical devices have been investigated in previous publications.[13,15,16,34,35] In this paper we extend these studies, using a different approach based on quantum scattering theory, relying on the exciton model of excitations.[36,37] We work in the weak damping limit and neglect dephasing and energy decay mechanisms.

Consider first two identical spherical nanodots. The radius-vector connecting the two dots is **R**. The distance is large, so two approximations apply. First, the overlap of the low-lying electronic eigenfunctions corresponding to two different dots is small and is set equal to zero: there is no electron sharing. Second, R^{-1} is small enough so the dipole

a)Author to whom correspondence should be addressed.
b)Electronic mail: roi.baer@huji.ac.il
c)Electronic mail: dxn@chem.ucla.edu

TABLE I. Values of parameters used in the 2D dynamics calculations.

Grid	Wave packet	V_I	V_{step}
$N_x = N_y = 30$	$\mathbf{k} = (-2, -2)$	$x_L = y_B = x_{step} = 16$	
$a = 1.0$	$\mathbf{r}_0 = (12, 12)$	$x_R = y_T = \Delta v = 0.8$	
$\xi = 1.0$	$\sigma = 1.2$	$\Gamma = 0.63$	

coupling term (proportional to R^{-3}) dominates the EM coupling between the dots. The dot we denote as 1 has a ground state Φ_1 and three dipole connected degenerate excited states Ψ_{1x}, Ψ_{1y}, and Ψ_{1z}. The corresponding states of dot 2 are Φ_2 and $\Psi_{2\alpha}$ $\alpha = x, y, z$. The $\Phi_i \rightarrow \Psi_{i,\alpha} (i = 1, 2)$ transition dipole is denoted ξ (here we assume a spherical symmetry, so ξ is independent of α). The ground state of the combined two-dot system is well approximated by $\Phi_1 \Phi_2$, while the low-lying excited states form a six-dimensional manifold, spanned by $\Phi_1 \Psi_{2\beta}$ and $\Psi_{1\alpha} \Phi_2$, $\alpha, \beta = x, y, z$. The 6×6 matrix representing the Hamiltonian in this space is

$$\langle \Phi_1 \Psi_{2\alpha} | \hat{H} | \Phi_1 \Psi_{2\beta} \rangle = \langle \Psi_{1\alpha} \Phi_2 | \hat{H} | \Psi_{2\beta} \Phi_2 \rangle = E_1 \delta_{\alpha\beta},$$

$$\langle \Psi_{1\alpha} \Phi_2 | \hat{H} | \Phi_1 \Psi_{2\beta} \rangle \equiv E_{\alpha\beta}(\mathbf{R}) = \xi^2 \frac{R^2 \delta_{\alpha\beta} - 3R_\alpha R_\beta}{R^5}. \quad (2.1)$$

Because R^{-1} is small, the eigenvalues of the matrix are all concentrated in a narrow band around the value of E_1 (E_1 is an additive constant and is set equal to zero with no loss of generality in our approximation). We concentrate only on the lowest excited states, so the theory is valid in the weak excitation limit.

Now, the two-dot system can be generalized to an N dot system with similar assumptions and approximations. The location of dot $i = 1, \ldots, N$ is $\mathbf{R}_i$, and we only treat the case of large interdot separation ($|\mathbf{R}_{ij}| = |\mathbf{R}_i - \mathbf{R}_j|$ large) as before. The low-lying excitation manifold is a Hilbert space spanned by $3N$ functions $\Psi_I \equiv \Psi_{i,\alpha}$ indicating the probability amplitude that the excitation is on site i in direction α ($I = (i\alpha)$ is a composite index). The real and symmetric Hamiltonian matrix is then

$$H_{IJ} \equiv H_{i\alpha, j\beta} = E_{\alpha\beta}(\mathbf{R}_{ij})(1 - \delta_{ij}). \quad (2.2)$$

A schematic of the type of systems we want to treat is shown in Table I.

We still need to take into account the infinite nature of nanodot wires leading into or out of the interaction region, i.e., the "leads" (Fig 1). In general we can have several leads. We denote their number by L. Of course, in any actual simulation the leads cannot be infinite: they are necessarily finite. Thus, supplement each lead by a negative imaginary potential (NIP) whose role is to absorb the wave packet[38,39] and prevent it from reflecting at the finite edge of the lead and return into the device. Consider such a lead we denote by l ($l = 1, \ldots, L$). Suppose the asymptotic direction of the lead (away from the system) is the unit vector $\mathbf{n}_l$ and its furthest edge is at point $\mathbf{R}_l$. Then the form of the NIP for this lead is $V^l_{i\alpha, j\beta} = \delta_{\alpha\beta} \delta_{ij} V^l_i$, with
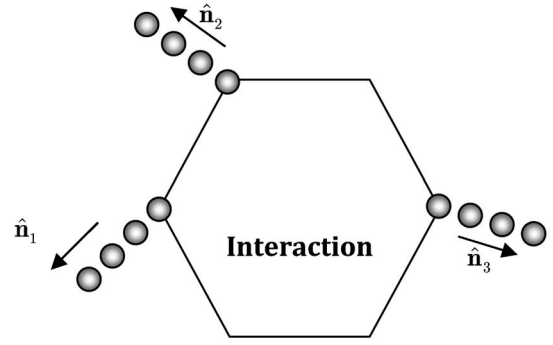

FIG. 1. A schematic picture of the system: an interaction or scattering zone, where a "polariton device" is found. The device is connected to one or more "infinite" wires called leads.

$$V^l_i \equiv v_{\text{NIP}}((\mathbf{R}_l - \mathbf{R}_i) \cdot \hat{\mathbf{n}}_l, |\mathbf{R}_l - \mathbf{R}_i|), \quad (2.3)$$

where

$$v_{\text{NIP}}(s, S) = -i\Gamma(\Lambda - s)^3 \theta(\Lambda - s) \times \theta(R - \sqrt{S^2 - s^2}). \quad (2.4)$$

Here, $\theta(x)$ is the Heaviside function, and we found by trial and error that the following parameters for the NIP are appropriate

$$\Gamma = 0.001, \quad \Lambda = 15R. \quad (2.5)$$

The total NIP is obtained by summing over all leads (summing on $l = 1, \ldots, L$), and we then add the resulting matrix to the Hamiltonian. We now consider the Hamiltonian H_{IJ} as the Hamiltonian which *includes* the NIP.

Wave Packet analysis: Example

Once the Hamiltonian is built, the dynamics of wave packets can be studied. One can define a Cartesian position matrix r^γ ($\gamma = x, y, z$),

$$r^\gamma_{IJ} = \delta_{IJ}(\mathbf{R}_i)_\gamma, \quad (2.6)$$

and a corresponding velocity

$$v^\gamma = i[H, r^\gamma]. \quad (2.7)$$

Furthermore, the density operator is

$$\rho(I)_{JK} = \delta_{IJ} \delta_{IK}, \quad (2.8)$$

so that the current density matrix is

$$j^\gamma(I)_{JK} = \tfrac{1}{2} \{(v^\gamma)_{JK'} \rho(I)_{K'K} + \rho(I)_{JK'}(v^\gamma)_{K'K}\}$$
$$= \tfrac{1}{2}(\delta_{IK} + \delta_{IJ})(v^\gamma)_{JK}. \quad (2.9)$$

These matrices help analyze the polariton wave packet dynamics in the system. Let us consider a wire of N dots and construct a wave packet $\psi_k = \sum_{n=1}^{N} [X_n \Psi_{n,x} + Y_n \Psi_{n,y}]$ (the coefficients X_n and Y_n indicate the probability amplitude for the excitation to be on site $\Psi_{n,x}$ and $\Psi_{n,y}$, respectively). To be specific, let us study closely an example, the scattering of a wave packet off a barrier. In a horizontal wire there is no coupling between longitudinal and vertical waves. However, a single dot vertically displaced from the wire breaks this symmetry and effectively forms a barrier (see the nanodot
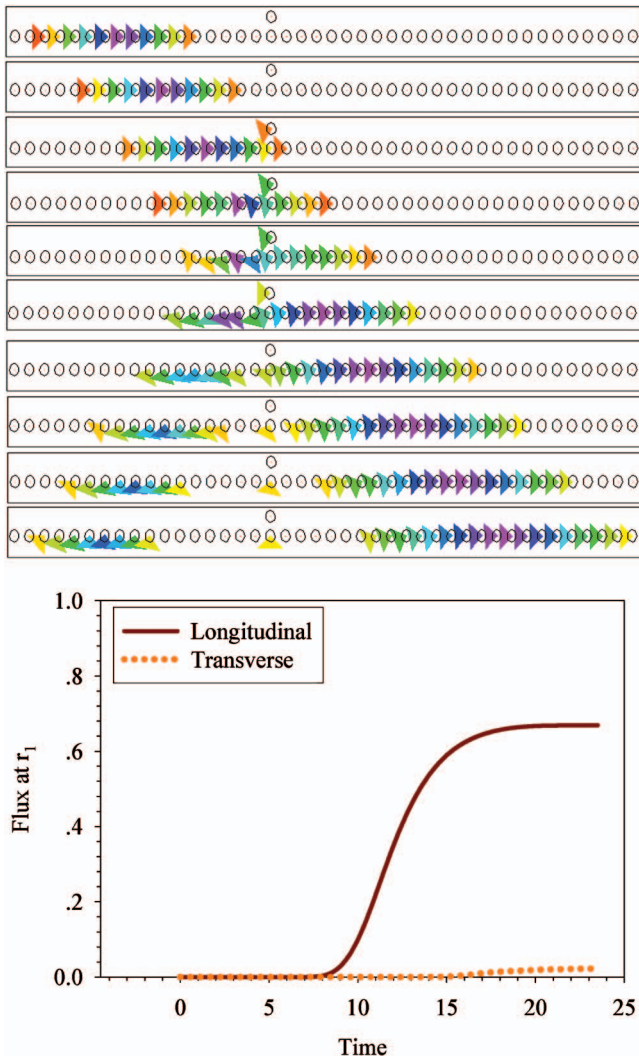
FIG. 2. (Color) Top: Polariton wave packet dynamics: each circle is a nanodot. A colored arrowhead indicates the direction and amplitude of the dipole excitation. For details consult text. Bottom: The flux going into the right lead after the scattering event.

configuration in Fig. 2). We consider this displaced dot to be the barrier. Choosing a longitudinal initial wave packet with wave vector k,

$$X_n = e^{-(n - n_0)^2/2\sigma^2} e^{ikRn}, \quad Y_n = 0, \tag{2.10}$$

and $\sigma = 2\pi/k$, allowing it to scatter off this barrier. Propagating the wave packet in time, the solution is

$$\psi_k(t) = e^{-iHt}\psi_k. \tag{2.11}$$

The probability $T_{x \to \alpha}$ to obtain a longitudinal or a transverse transmitted wave can be measured by integrating the current density over time,

$$T_{x \to \alpha} = \int_0^\infty J_\alpha(r_1, t')dt'. \tag{2.12}$$

A graphical view of the resulting dynamics is shown as snapshots at equal time intervals in Fig. 2. In the calculation we took $\xi = R = D = 1$ and $k = 2$. The time interval between snapshots is one unit of time. In the figure, each site is represented by a circle. If site n has a probability of being excited,

we denote this by an arrowhead. The arrow points in the direction $(|X_n|^2, |Y_n|^2)$ and its color indicate the amplitude of excitation, $a_n = |X_n|^2 + |Y_n|^2$, using a rainbow scaled legend. Purple is assigned to max a_n, while red indicates an amplitude smaller by a factor of ~ 7. Amplitudes below this value are not indicated with an arrowhead.

Observing Fig. 2, we see the initial longitudinal wave packet advancing with velocity of about three units. Once it impinges on the barrier, part of the wave packet is transmitted and another part is reflected. It is interesting to observe that most of the transmitted waves are longitudinal while most of the reflected waves are transverse. Indeed, using the flux, shown in Fig. 2 (bottom), we find that transmitting a longitudinal wave packet has a probability of 0.67 while transmitting a transverse wave packet is much less probable, at only 0.03. On the other hand, a large portion of the reflected wave packet (probability of about 0.23) is transverse while only a small part is longitudinal (0.07). Another noticeable effect in Fig. 2 is that the velocity of the reflected wave packet is approximately two units, considerably smaller than the velocity of the incoming or transmitted wave packet. In the next section we describe the dispersion relations of polaritons on the wire. These allow understanding of most of the observed feature in Fig. 2, except the amount of transmission or reflection, which usually is difficult to explain and requires explicit calculation.

Dispersion of waves on a 1D Wire

In this section, we consider theoretically the one-dimensional (1D) infinite straight wire with active centers placed along the x axis at a spacing of R. From Eq. (2.2) the Hamiltonian is

$$H_{n,m} = \frac{A}{|n - m|^3}, n \neq m, \tag{2.13}$$

where the coupling constant depends on the type of wave, transverse or longitudinal,

$$A_T = \frac{\xi^2}{R^3}, \quad A_L = -2A_T. \tag{2.14}$$

Standard Ewald-type methods can be applied for the system. They imply that for an infinite lattice, the eigenenergy is a function of the wave vector $k \in [-\pi/R, \pi/R]$ and of R, given by

$$\omega_k = 2Af_3(kR), \tag{2.15}$$

where

$$f_m(x) = \sum_{n=1}^\infty \frac{\cos(nx)}{n^m}. \tag{2.16}$$

We see that $R^3\omega_k$ is a function of kR. This function, denoted as $f_3(kR)$ converges for all values of kR. However, its second derivative $-f_3''(x) = f_1(x) \equiv \Sigma_n \cos(nx)/n$ is divergent at $x \to 0$, where it behaves like $(x^2/4)\ln x^2$. The remainder is well behaved and can be expanded in a Taylor series,
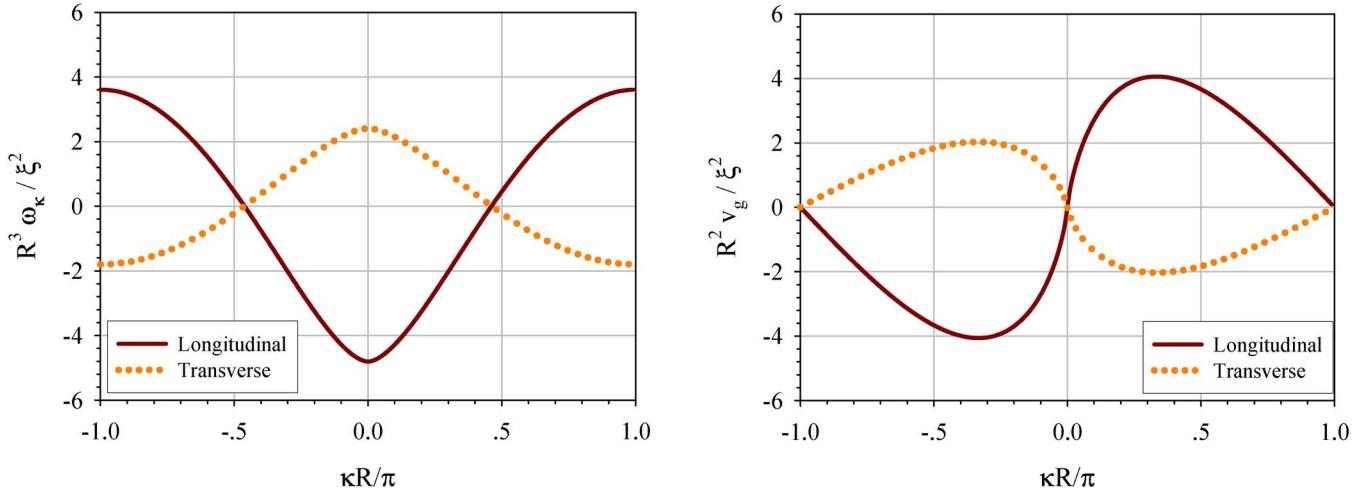
FIG. 3. (Color online) Dispersion relations (left) and group velocities (right) for the waves on an infinite equally spaced lattice.

$$f_3(x) = Z(3) + \frac{1}{4}(\ln x^2 - 3)x^2 - \frac{x^4}{288} - \frac{x^6}{86\,400}$$

$$- \frac{x^8}{10\,160\,640} + \cdots , \qquad (2.17)$$

where $Z(z)$ is the Riemann zeta function ($Z(3) = 1.202\,06\ldots$). This approximation becomes indefinitely exact as $x \to 0$. When $0 < x \lesssim \pi$ the maximal error is 2×10^{-4}. For most purposes, an accuracy of 0.02 is reasonable and it is possible to neglect terms beyond the $(kR)^4$. We thus assume henceforth the following dispersion relation:

$$\frac{\omega_k}{2A} = f_3(kR) \approx Z[3] + \left(\frac{\ln|kR|}{2} - \frac{3}{4}\right)(kR)^2 - \frac{(kR)^4}{288}.$$

$$(2.18)$$

The dispersion relation for the longitudinal and transverse waves is shown in Fig. 3. This curve is very similar to the dispersion found for five-nearest neighbor small damping limit.[15] The harmonic model[15] can be shown to be equivalent to the present model in the weak field limit, so this is hardly a surprise. The bandwidth for transverse waves is half that of the longitudinal waves. Indeed, the longitudinal waves have a minimum energy at $k=0$ of $-4.8A_T$ (where $A_T = \xi^2/R^3$) and a maximal energy of about $3.6A_T$ at $k=\pi/R$. The transverse energy is minimal, $-1.8A_T$ at $k=\pi/R$, and maximal, $2.4A_T$, at $k=0$. We see that the longitudinal band spans an energy interval twice that of the transverse band. An important feature is that both types of waves obtain zero energy at the *same* wave vector $k_0 \approx \pm 0.46\pi/R$. This has an important implication for the scattering properties of these waves, as discussed in the next section. The slope of the dispersion curve is the group velocity, and gives the relation between the wave vector (or the energy) and the actual velocity of the EM energy,

$$v_g = \frac{d\omega_k}{dk} \approx -2AR^2k\left((1 - \ln|kR|) + \frac{(kR)^2}{72}\right). \qquad (2.19)$$

This velocity is shown in Fig. 3. We see that longitudinal waves move in the same direction as the wave vector k, yet the transverse waves move in the opposite direction. This

fact too will have an implication on the scattering properties of the system. One should note that the slope of the group velocity at $k=0$ is infinite. This shows that the effective mass

$$\mu_{\text{eff}} = \left(\frac{dv_g}{dk}\right)^{-1} \approx \left(-2AR^2\left(\frac{(Rk)^2}{24} - \ln(Rk)\right)\right)^{-1} \qquad (2.20)$$

converges logarithmically to zero at $k=0$. This singular behavior is a result of the infinite range of the dipole interaction (which decays only algebraically) and will not be seen in a nearest neighbor model. The significance of this divergence is evident only in extremely long wires, where this weak singularity can accumulate. In practice, under usual conditions, we do not expect that such conditions will prevail due to the existence of disorder and dephasing and in long wires retardation effects, all of which are neglected here, although an unusually small effective mass will be seen for finite lattices at long wavelengths.

Using the dispersion and group velocities in Fig. 3, we can explain many of the features found in the example of wave packet dynamics shown in the previous section. First, we can explain the velocity of the longitudinal wave packet, which is 3. This is because the group velocity corresponding to $k=2$ is indeed 3. Then we need to explain the fact that most of the transverse waves are reflected, i.e., have a negative velocity of about -2. In the scattering event the energy is conserved so far from the scatterer; the reflected wave has the same energy as the impinging wave. From the dispersion curve (Fig. 3), the energy corresponding to $k=2$ is $\omega=1$. The transverse waves thus formed must have $k=\pm 0.25$. It is reasonable that k does not change sign. Thus the wave vector of the transverse wave is 0.25, which corresponds to a velocity of -2. What the dispersion curves cannot tell us is the probability for various events. For this, there is no alternative but a dynamical calculation.

Energy-polarization resolved scattering approach

We now describe a time-independent Green's function approach that enables an efficient calculation of the various scattering probabilities as a function of energy. We specialize in systems where the nanodots are all contained in a single
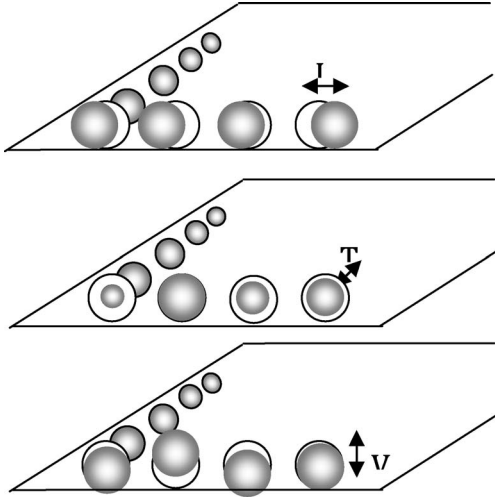
FIG. 4. Three types of polariton waves: longitudinal (L) along the wire, transverse (T) perpendicular to the wire but in the plane and vertical (V) perpendicular to the plane. The circles are schematic representation of the ionic cores of the dot and the gray shadows represent the oscillating electron clouds.

plane. The polaritonic waves in any lead l are thus of three different types of polarizations (the reader may consult the schematic illustrations in Fig. 4): *longitudinal*: when the polarization is in the direction $\hat{\mathbf{n}}_i$, *transverse*: when the polarization is in the nanodot plane but orthogonal to $\hat{\mathbf{n}}$, and *vertical*: when the polarization is perpendicular to the nanodot plane. Denote by $P_{(l,\alpha)\rightarrow(l',\alpha')}(E)$ the cumulative probability for incoming waves of energy E and polarity α (where $\alpha = L, T, V$) in lead l to scatter out to lead l' in polarity α'. The negative imaginary parts of the leads l and l' can be used to compute $P_{(l,\alpha)\rightarrow(l',\alpha')}(E)$. We define a suitably projected T matrix as follows:

$$T = 2\Gamma_{l\alpha}G(E)\Gamma_{l'\alpha'}, \tag{2.21}$$

where

$$(\Gamma_{l\alpha})_{i\beta,j\gamma} = \delta_{ij}\delta_{\alpha\beta}\sqrt{V_i^l}(\wp(\hat{\mathbf{n}}_l))_{\beta\gamma},$$
$$\wp(\hat{\mathbf{n}}) = \begin{pmatrix} n_x^2 & -n_x n_y & 0 \\ -n_x n_y & n_y^2 & 0 \\ 0 & 0 & 1 \end{pmatrix}. \tag{2.22}$$

Using the Seideman-Miller trace expression for transmission,[40] one then obtains

$$P_{(l,\alpha)\rightarrow(l',\alpha')}(E) = \mathrm{Tr}[T(E)^\dagger T(E)]. \tag{2.23}$$

Each of the negative imaginary potentials V^l [see Eqs. (2.3)–(2.5)] must ideally be nonreflecting and fully absorbing in their corresponding asymptotic channels (leads) for Eq. (2.23) to be valid. This is because only then do these potentials act like the outgoing flux (surface integrated current density) operator across the boundary surface between the system and the lead.[39]

Since the system is not large, it is more efficient to first diagonalize the Hamiltonian and work out the trace in the diagonal representation. The diagonalization is one (expensive) operation scaling as the cubic number of sites $O(N^3)$. After that, however, each trace calculation can be set up to cost $O(N^2)$ operations.

Dynamics on a 2D lattice

While this paper is concentrated more on one-dimensional channels, we touch briefly in this section on two-dimensional (2D) lattices of nanoparticles. We consider a lattice of $N = N_x N_y$ particles, with nearest neighbor spacing a. We consider a vertical excitation. This type of excitation does not couple to in-plane (longitudinal or transverse) modes. For this, we do not need the full Hamiltonian given in Eq. (2.2), but only the part that relates to vertical waves. For a completely "vertical" initial Gaussian wave packet of width σ, centered $\mathbf{r}_0$ with wave vector $\dot{\mathbf{k}}$,

$$\psi(\mathbf{r};0) = e^{-|\mathbf{r}-\mathbf{r}_0|^2/2\sigma}e^{i\mathbf{k}\cdot(\mathbf{r}-\mathbf{r}_0)} \tag{2.24}$$

the in-plane modes are neglected, and the behavior of the system can be completely described by the $N \times N$ Hamiltonian,

$$H_{nm} = \begin{cases} \nu, & n = m \\ \dfrac{\xi^2}{R_{nm}^2}, & n \neq m, \end{cases} \tag{2.25}$$

where, for clarity, we have dropped the z subscript and, like before, ν is the surface plasmon transition frequency of the nanoparticles.

We impose a quadratic negative imaginary potential, resulting in an absorbing "rim" around the grid. This potential is given by

$$V_I^{nm} = \delta_{nm}[v_I(x_L - x_n) + v_I(x_n - x_R) + v_I(y_B - y_n) + v_I(y_T - y_n)], \tag{2.26}$$

where (x_n, y_n) is the position of the nth nanoparticle and

$$v_I(p) = \Gamma p^2 \theta(p). \tag{2.27}$$

The various parameters of the potential are given in Table I. The grid was then divided into two slabs by stepping the transition frequency $\nu \rightarrow \nu + \Delta\nu$ for $x \geq x_{\mathrm{step}}$, thus creating a barrier of the form

$$V_{\mathrm{step}}^{nm} = \delta_{nm}\theta(x - x_{\mathrm{step}})\Delta\nu, \tag{2.28}$$

where $\theta(x)$ is the Heaviside step function.

Finally, the wave packet was evolved according to

$$\psi(\mathbf{r};t) = e^{-i\bar{H}t}\psi(\mathbf{r};0), \tag{2.29}$$

where $\bar{H}$ is the complex-symmetric effective Hamiltonian

$$\bar{H} = H + V_{\mathrm{step}} - iV_I. \tag{2.30}$$

Figure 5 shows snapshots, taken at different times, of the wavepacket on a 30×30 lattice. with the various adjustable parameters chosen as shown in Table I. The color contour plots represent the probability of a nanoparticle at that position being excited, with red representing probabilities greater than 0.15. The first feature of note is that analogous to the
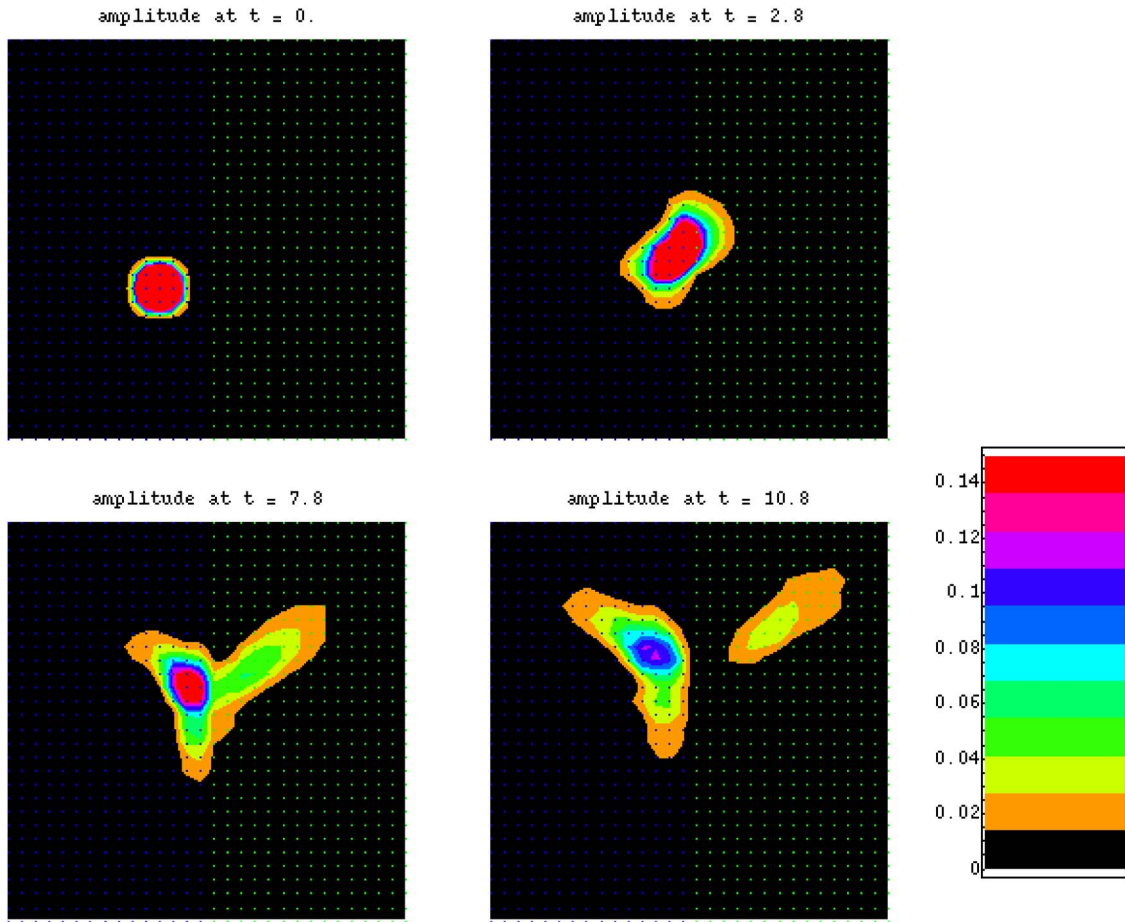
FIG. 5. (Color online) Snapshots of LSPP dynamics on a 30×30 nanoparticle lattice. LSPP amplitude is color scaled. The initial LSPP starts in a region of frequency ν (blue dots), moving in the north-east direction. It subsequently collides with the region of plasmon frequency $\nu + \Delta\nu$ (green dots). The wave breaks into refracted and reflected parts.

transverse waves in 1D, the group velocity of the 2D wave-packet is antiparallel to **k** for this particular choice of initial momentum ($k_x = k_y = -2.0$). It is observed that the group velocity in the x and y directions can range from negative to zero to positive depending on the value of **k**, as is expected from a dispersive medium such as this.

Upon striking the barrier, part of the wave packet is transmitted while part is reflected; the relative proportion and shape of the wave packet reflected vary strongly with $\Delta\nu$. It is interesting to find that the wave packet slides along the interface before reflection and refraction occur. In a future publication we will study the "optics" of such encounters, using the 2D dispersion relation of the system.

DEVICES FOR COHERENT PLASMONICS

Basic scattering obstacles

Polariton waves along a straight wire with equally spaced nanodots simply propagate within the allowed energy band, between -4.8 and 3.6 for longitudinal and transverse waves. This is seen in Fig. 6(a). Three basic types of obstacles can be formed on such a wire, as shown in Fig. 6(b), $\xi - \xi'$ coupling where the transition dipole moment is changed, (c) $R - R'$ coupling where the spacing between the

nanodots is changed, and (d) $\nu - \nu'$ coupling where the transition frequency is changed. Consider then a polariton of wave vector k and energy ω_k coming from a wire with transition dipole moment ξ and passing into a wire with transition dipole $\xi' < \xi$ (for definiteness). In the wire, the energy ω_k is limited to the band $\omega_k \in 2A[f_3(\pi), f_3(0)]$. Since $A \propto R^{-3}$, we find that the band in the second wire is changed by proportion,

$$[\omega'_{min}, \omega'_{max}] = \left(\frac{\xi'}{\xi}\right)^2 [\omega_{min}, \omega_{max}]. \tag{3.1}$$

If the energy of the wave ω_k is outside of this window it will not be able to be transmitted into the new wire and there will be total reflection. If the energy is in this interval, then since it is conserved, we must have

$$\xi^2 f_3(kR) = \xi'^2 f_3(k'R). \tag{3.2}$$

Thus, the wave vector k must change to k' to accommodate the change in coupling strength. This change in wavelength can in general cause loss of transmittance or increased reflectance. Since the value $\omega = 0$ is contained in the original interval (ω_{min} is negative while ω_{max} is positive), there is always, in principle, an energy window around $\omega = 0$ through which
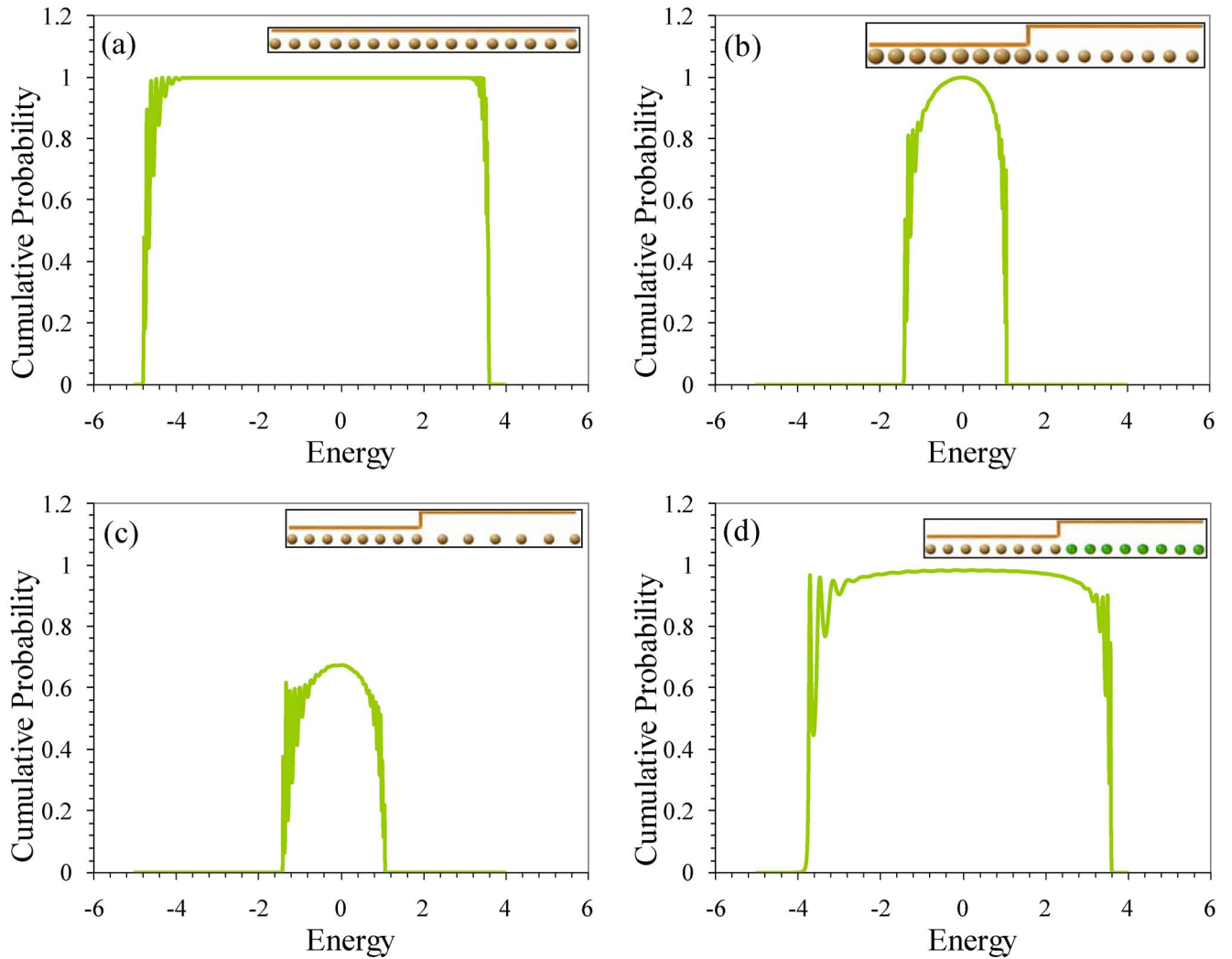
FIG. 6. (Color online) The transmission probability through (a) a straight equally spaced wire, (b) an $R \rightarrow R' = 3/2$ step, (c) a $\nu = 0 \rightarrow \nu' = 1$ step, and (d) a $\xi = 1 \rightarrow \xi' = (2/3)^{3/2}$ step. The inset in each graph is a schematic of the corresponding barrier.

waves can pass. Furthermore, at this energy $f_3 = 0$, so the condition (3.2) necessarily means

$$\omega_k = 0 \Rightarrow kR = k'R. \tag{3.3}$$

Thus, there is no change in wavelength. The transmittance here is therefore accomplished with probability 1. This is a very important property for this type of barrier: there is always an energy window, no matter how narrow through which the wave can pass. We can see this numerically when we examine the case $R = R' = 1$, $\nu = \nu'$, and $\xi' = (2/3)^{3/2}\xi$ in the calculated transmission curve [Fig. 6(b)]. The analysis above is borne out: the nonzero longitudinal transmission is limited to an interval which is $8/27[-4.8, 3.6]$, exactly in accordance with Eq. (3.1). Furthermore, the transmission probability near $\omega = 0$ is indeed 1. A similar correspondence is seen for the transverse waves.

Now consider a similar situation where the spacing between the nanodots changes from R to $R' > R$. Now the nonzero transmission interval is given by

$$[\omega'_{min}, \omega'_{max}] = \left(\frac{R}{R'}\right)^3 [\omega_{min}, \omega_{max}]. \tag{3.4}$$

Again, since the value $\omega = 0$ is contained in the original interval there is always, in principle, an energy window around this value through which waves can pass: this type of barrier cannot block all waves. The wave vector changes according to

$$R^{-3}f_3(kR) = R'^{-3}f_3(k'R'). \tag{3.5}$$

In this case, even for $\omega = 0$ there is a change of wave vector, since we have

$$\omega_k = 0 \Rightarrow, \quad kR = k'R'. \tag{3.6}$$

Thus, even at $\omega = 0$ there is a change of wavelength and we cannot expect in general that the transmission probability at $\omega = 0$ will be unity, as in the previous case. Once again, this analysis is borne out in the numerical examples, as shown in Fig. 6(c). Here we take $R' = (3/2)R$ and $\xi = \xi'$. The energy interval is once again $8/27$ times the original interval, but the transmission probability is less than unity at $\omega = 0$. Finally, we study the case of $\nu \rightarrow \nu' = \nu + 1$. In this case there is a
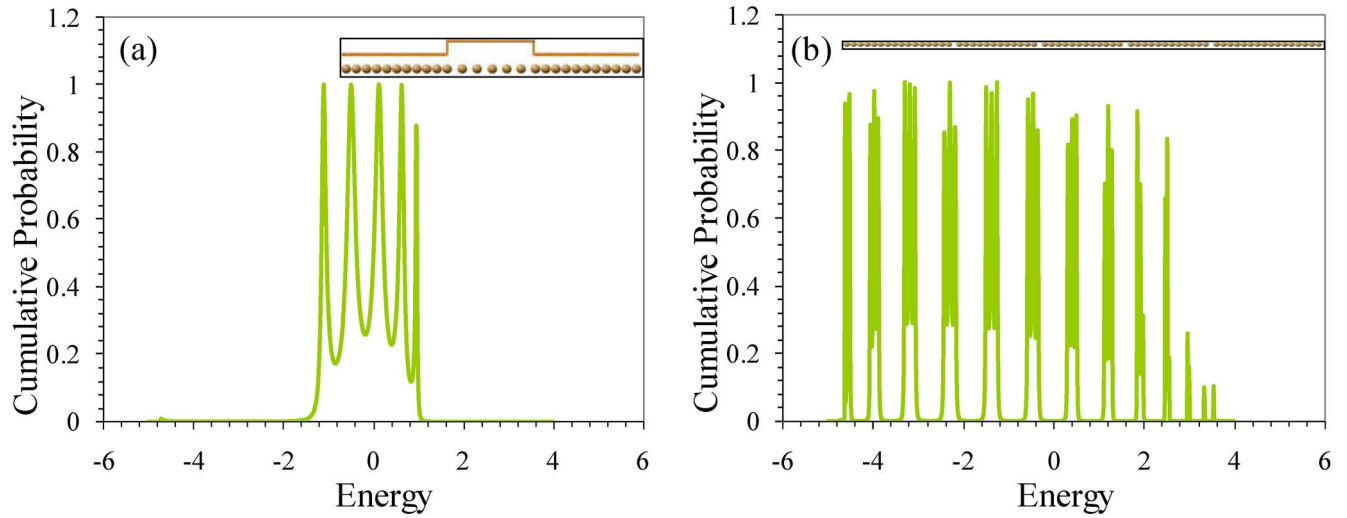
FIG. 7. (Color online) The transmission probability through (a) single and (b) multiple barriers.

smaller band of transmittance, but the analysis is not as straightforward.

We move on to consider step barriers of finite extent. The bandwidth scaling of Eq. (3.2) or (3.4) is an important tool for understanding and estimating the effects of finite square barriers similar to the one shown in the inset of Fig. 7. Consider, for example, the transmission probability through such a barrier of width $6R'$ (where $R=1$ and $R'=1.5$), as shown in the inset of Fig. 7. The transmission is substantially nonzero only in an interval of energy very similar in width to the interval for a semi-infinite wire [Fig. 6(c)]. Thus the width is easily predicted by the scaling of Eq. (3.4), even for a relatively thin barrier. Note that the shape of the transmission is difficult to predict exactly. The width of the barrier determines the number of resonance peaks. In the present case, the transmission curve has five sharp peaks corresponding to the five sites of the barrier.

From the discussion above, it may seem that the $\omega=0$ component is able to penetrate just about any barrier. However, this is not true in general. Indeed, interference through multiple barriers creates alternating energy bands of reflected and transmitted waves. In Fig. 7(b) we see the formation of such bands in the transmission function through four equally spaced barriers. Each barrier is formed by increasing the spacing from R to $1.5R$. The distance between two consecutive barriers is $12R$. This latter width determines the number of energy bands [Eq. (12)], while the number of peaks in each band is equal to the total number of barriers minus 1. Thus, if the number of barriers is increased indefinitely, the transmitting bands will form continua, roughly equal in width to band barriers shown in Fig. 7(b). The $\omega=0$ waves are within the total reflection band in this example.

Acceleration of wave packets

In order to create and manipulate wave packets, we need to be able to control their momentum (wave vector) and velocity. This can be done by creating a slope, i.e., a gradual

decrease or increase in grid spacing. For example, consider longitudinal waves in an infinite array with the spacing between consecutive nanoparticles given by

$$\rho_n = R \begin{cases} \dfrac{e^{gn} + \eta}{1 + \eta}, & n > 0 \\ 1, & n \leq 0. \end{cases} \tag{3.7}$$

Here, R is the initial spacing (taken as 1 in our units) and g is the rate of change of the spacing ρ_n. η determines the minimal spacing and is typically much smaller than 1 (ηR is actually the diameter of the nanoparticle and R is initially much larger than ηR). When g is positive, the spacing grows down the positive direction, and when it is negative, the distance between nanoparticles progressively becomes smaller. In Fig. 8 we show the velocity and acceleration expectation values as functions of time for a longitudinal wave packet of initial group velocity of 3.88 at several values of g. Initially, the wave packet starts in the negative n part [see Eq. (3.7)] where the spacing between nanoparticles is constant. As it moves into the region of varying spacing, the wave packets starts to "feel" the attraction or repulsion forces, and its velocity expectation value changes accordingly. The initial velocity value of 3.88 corresponds to $Rk_0=0.46\pi$, the wave vector for which $\omega_{k_0}=0$. Choosing this value makes the semiclassical analysis in the Appendix considerably easier. This semiclassical analysis can explain the short-time quantum behavior shown in Fig. 8. We obtain the following expression for the group velocity as a function of time:

$$\frac{1}{v_g(t)} = \frac{1}{v_g(0)} + 2g \int_0^t \frac{dt}{\rho(t)}. \tag{3.8}$$

This seems to fit well the quantal calculations for small t. For negative g the semiclassical analysis predicts that the velocity will diverge to infinity at some finite critical time for which the right hand side of Eq. (3.8) vanishes. In the quantal calculations we do not find a divergence but a strongly increasing acceleration as time proceeds.
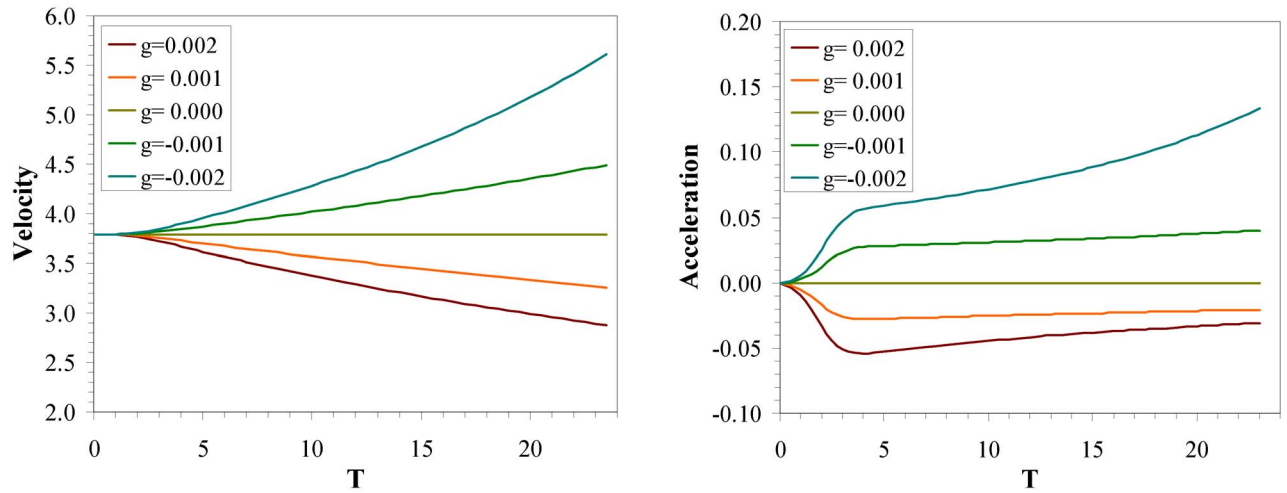
FIG. 8. (Color online) Wave packet calculation as discussed in the text, showing the velocity (left) and acceleration (right) as a function of time for several values of the parameter g in an array with nanodot positions as given by Eq. (3.7). The initial wave vector is $k=0.46\pi$ and $\eta=0.1$ was used.

Longitudinal-transverse conversion

In the previous subsection, we concentrated on straight wires which due to their intrinsic cylindrical symmetry do not couple the transverse and longitudinal modes. We now want to look at more complicated cases, where part of this symmetry is removed. A device that can help manipulate the polarity (whether longitudinal of transverse) of the waves is extremely important. One simple way to do this, as we saw in the section on devices for plasmonics, is to put a nanodot near a waveguide. Such a construct, we saw, will cause the reflected waves to change polarity. We now investigate this issue further and show that there exist energy intervals where the waves are purely longitudinal and cannot be converted. On the other hand, in other intervals such a conversion has an efficiency which can exceed 50%..

Consider first the example in the section on wave packet analysis, namely, scattering through a barrier. The energy resolved calculation shows clearly what we saw also in the wave packet calculation (see Fig. 2). We first analyze the scattering of the vertical waves, since they do not couple to the other types of polarization waves in this planar system. Analytically, we consider one limit—when D is very large. In this case, the added nanodot will be coupled only weakly to the system, and so only the waves with zero energy will be affected (since the energy of a single dot is $\omega=0$). Thus we need only consider three states of the waves traveling from left to right $\psi_R=e^{ik_0n}$, from right to left $\psi_L=e^{-ik_0n}$ (where $Rk_0=0.46\pi$ is the wave vector corresponding to zero energy, see Fig. 3), and the wave ψ_D localized on the additional site. The Hamiltonian matrix of this 3×3 system is of the form $\begin{pmatrix} 0 & 0 & c \\ 0 & 0 & c \\ c & c & 0 \end{pmatrix}$, where c is a real constant depending on D and k_0,

$$c = \xi^2 \left[\frac{1}{D^3} + 2\sum_{n=1}^{\infty} \frac{\cos kn}{((Rn)^2 + D^2)^{3/2}} \right]. \tag{3.9}$$

This system has three nondegenerate eigenvalues (0 and $\pm\sqrt{2}c$) and therefore its three stationary wave functions nec-

essarily have no flux associated with them, $\phi_0=(1/\sqrt{2})(\psi_L - \psi_R)$ and $\phi_\pm=(1/2)(\psi_L+\psi_R)\pm(1/\sqrt{2})\psi_D$. This means that there is always total reflection, as each wave going to the right must be accompanied by a wave moving to the left with the same probability. This situation prevails only in the limit where D is so large that only the above three states need to be considered. When D is finite, other nearby states are also necessary and the analysis becomes gradually invalid; i.e., scattering states can be formed.

Now consider what happens when we allow for longitudinal and transverse waves which can be coupled by the outstanding nanoparticle. Again, consider the large D limit, and now there are four waves $\psi_{L,\alpha}$ and $\psi_{R,\alpha}$, where α takes two values, L and T, indicating whether the wave is longitudinal or transverse. The excitation on the outstanding nanoparticle also has two polarization modes, so this time the Hamiltonian is reduced to a six-dimensional matrix and has the following structure:

$$H = \begin{pmatrix} 0 & \tau \\ \tau^\dagger & 0 \end{pmatrix} = \nu \begin{pmatrix} 0 & 0 & 0 & 0 & f & 1 \\ 0 & 0 & 0 & 0 & 1 & g^* \\ 0 & 0 & 0 & 0 & f^* & 1 \\ 0 & 0 & 0 & 0 & 1 & g \\ f^* & 1 & f & 1 & 0 & 0 \\ 1 & g & 1 & g^* & 0 & 0 \end{pmatrix}, \tag{3.10}$$

where ν, f, and g depend on D and k_0. τ is a 4×2 coupling matrix. We now analyze what eigenvalues can such a Hamiltonian admit. First, write down the eigenvalue equation as

$$\begin{pmatrix} 0 & \tau \\ \tau^\dagger & 0 \end{pmatrix} (X) = E(X). \tag{3.11}$$

Multiplying by H from the left, we obtain

$$\begin{pmatrix} \tau\tau^\dagger & 0 \\ 0 & \tau^\dagger\tau \end{pmatrix} (X) = E^2(X). \tag{3.12}$$

So we need to look for eigenvalues of $\tau\tau^\dagger$, which is a 4×4 matrix. But this matrix must have two zero eigenvalues because τ has a rank deficiency of 2. By numerically checking,
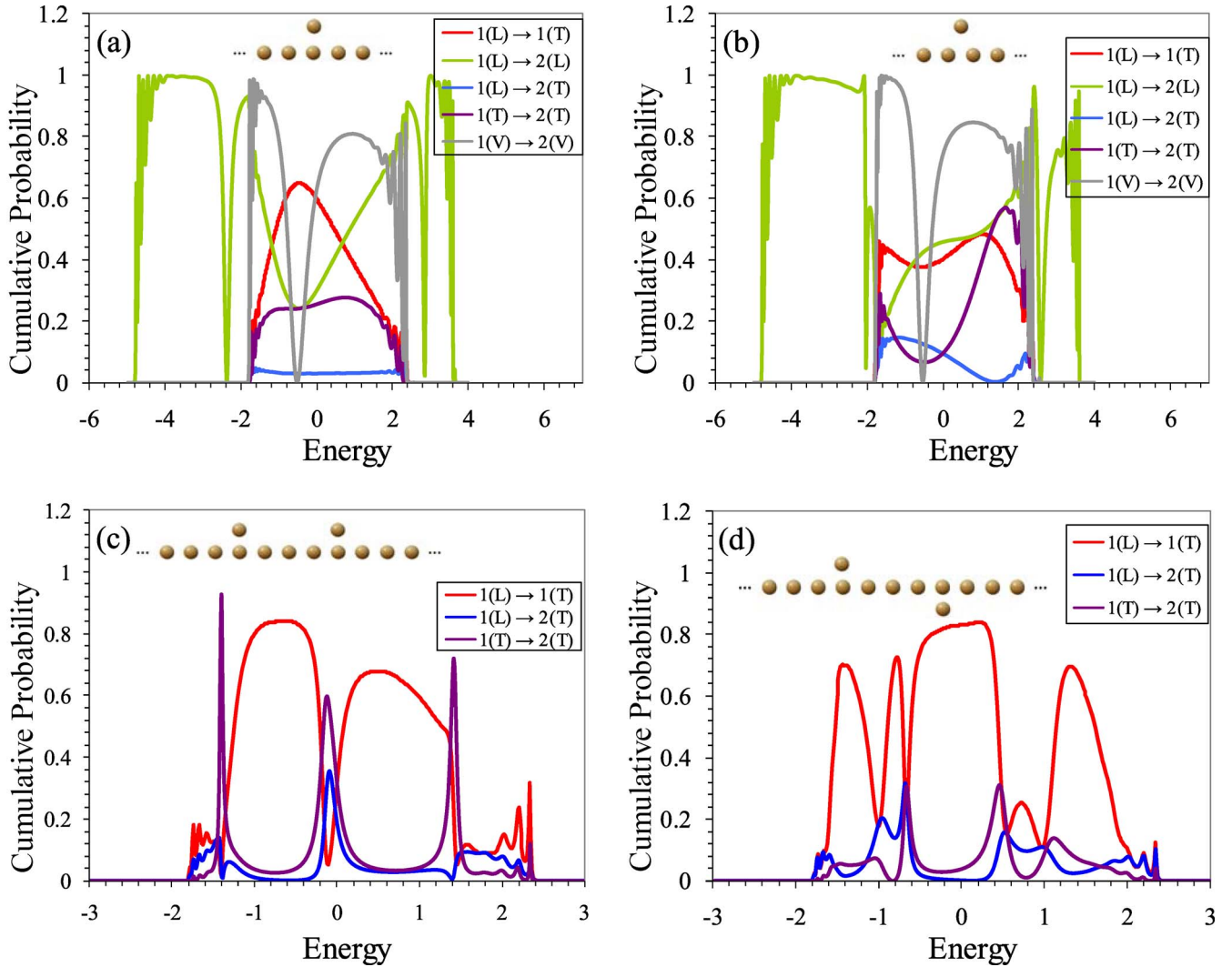
FIG. 9. (Color online) The scattering amplitudes through an infinite nanowaveguide with a single offset nanodot barrier. The barrier types are shown in the insets.

it is evident that the two other eigenvalues are in general nonzero, are different from each other, and are shared by $\tau^\dagger\tau$. We thus conclude that the $\omega=0$ eigenvalue is doubly degenerate, a situation which facilitates current carrying eigenstates. This allows nonreflecting solutions.

These analytical results serve to explain the behavior of the scattering properties but are, of course, very limited in their scope. We thus now show some results obtained by actually solving the scattering problem in a numerically exact way. These illustrate the rich properties of the dipolar waves, even in simple systems as considered here. In Fig. 9, we show the transmission through a barrier we discussed above. We see that there is a wide energy range where only longitudinal waves can exist, and these are usually transmitted through the wire unchanged, except at an antiresonance which may occur near the threshold for producing other polarizations. Once in the energy range where transverse waves can exist, an impinging longitudinal wave is transmitted as a longitudinal wave with probability of 20%–70% (mostly around 50%) depending on the energy. It can be transmitted as a transverse wave, although this has low probability, or it can be reflected as a transverse wave with probability close to

50% as well. If the impinging wave is transverse, it may have a large probability to go through as a transverse wave or be reflected as a longitudinal wave. This is a similar result to the time-dependent calculation.

The vertical waves cannot change their character because they are not coupled to the transverse or longitudinal waves. When D is larger they will exhibit a strong reflectance at $\omega=0$. In Fig. 9 we see that even when $D=1$ this is the behavior.

An interesting question is how to increase the efficiency of the conversion of waves from longitudinal to transverse (or the other way around). One way would be to use interference again, but this time constructive. Indeed, if we place two dots spaced by $4R$ at a distance $D=1$ from the wire, as in the inset of Fig. 9(c), we obtain increased conversion probabilities. We indeed see that at energies in a wide interval around $\omega=-0.8$ the reflective conversion probability exceeds 80%. Changing the spacing between the two nanodots to 4.3 serves to increase the efficiency of conversion further to well above 90%. It is interesting to note that the conversion in the forward direction is increased as well (around $\omega=0$) by this scheme. Narrow resonances allow transmission of transverse
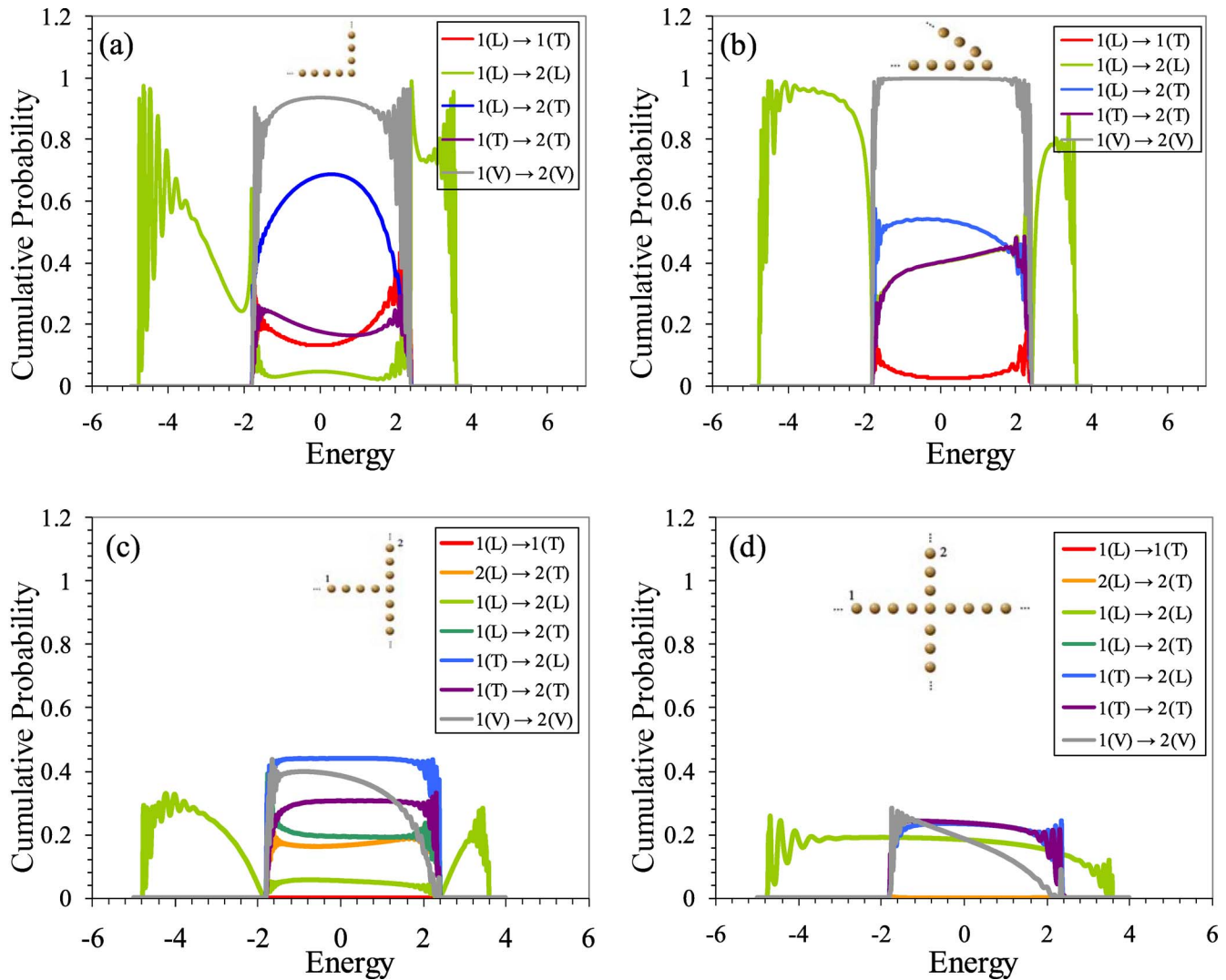
FIG. 10. (Color online) The probabilities of transmission and reflection in corners.

waves with high efficiency in this setup. Another way of placing the two dots is in an antisymmetric manner, as shown in the inset of Fig. 9(d). This changes the energy interval at which the increased conversion frequencies are seen.

Corners and Intersections

An important issue is the ability of waveguides to bend the direction of the traveling waves. Intuitively, it is clear that a simple right angle corner will change the polarity of the light if it is transverse or longitudinal. Figure 10(a) examines the scattering ensued by such a corner. It is seen that vertical waves suffer very little reflection (typically considerably less than 10%). Longitudinal waves, on the other hand, are transmitted with considerable probability (around 70%), but during this, they are converted to transverse waves, as would be expected. Transverse waves can take the corner and stay transverse more easily than longitudinal waves do. Finally, there is about 20% chance that the reflected wave will change character from longitudinal to transverse and vice versa.

When the corner angle is decreased to say 45°, as shown in Fig. 10(b), some properties change. The vertical waves

almost do not reflect at all from such a corner (except near the threshold). The efficiency of conversion from longitudinal to transverse as the wave is transmitted goes down to about 50%. The probability for the transverse wave to take the corner unchanged in character goes up to about 40%. Interestingly, the probability to be reflected with change in character is exactly equal to that for transmitting longitudinal waves without change of character.

SUMMARY AND DISCUSSION

We have described a scattering framework for analyzing the dynamics of polariton waves in wires and associated structures. Using the analytical and numerical methods so developed, we have studied several simple systems. Some of the results are simple enough to be explained using the analytical model and additional reasonable assumptions. Some of the results require more elaborate and accurate numerical methods.

The LSPP waves exhibit a rich variety of properties, which may be useful for future scientific developments and perhaps technological advances. By selecting energy ranges or geometries, we can isolate types of waves; for example,

longitudinal waves are the only waves that can exist at high and low energies. In the planar structures we considered, vertical waves are essentially decoupled from the two polarization waves and enjoy unique properties, such as the ability to take sharp turns with small reflectance. In the energy region where both transverse and longitudinal waves can coexist, the fact that they move in opposing direction for a given wave vector strongly dominates many of the properties we saw, especially those related to reflection and longitudinal-transverse conversion probability.

Future work must address important issues such as disorder and decoherence. Disorder in these systems will cause reduced transmission across finite barriers because of localization. Decoherence or dephasing is an important process in silver nanoparticles. Because the principal decoherence processes are localized in the nanoparticles, we expect that its principal effect on the wave dynamics is reducing the amplitudes of the waves. The energy lost by the coherent LSPP waves will eventually funnel into heating up the nanoparticles.

ACKNOWLEDGMENTS

APPENDIX: SEMICLASSICAL ACCELERATION

We discuss here the dynamics on an array where the dots become progressively more condensed. Equation (3.7) describes a linear condensation, the rate of which is determined by a parameter g. When a wave packet of wave vector k and energy $\omega = \omega_k(R)$ passes through such a lattice, assuming g is small so R does not change appreciably over the width of the wave packet, we can estimate the acceleration as follows. The energy must be preserved, so as the spacing ρ_n (we shall drop the subscript n where it causes no confusion) changes by $\delta\rho$, the principal wave must respond by a corresponding change in δk so that the energy stays, as it must, constant. Thus, the condition $0 = \omega(\rho + \delta\rho, k + \delta k) - \omega(\rho, k)$, from which follows

$$\delta k = -\frac{1}{v_g}\frac{\partial \omega_k}{\partial \rho}\delta\rho, \tag{A1}$$

where $v_g(\rho, k) = \partial\omega/\partial k$ is the group velocity. Using Eq. (2.15) we can show that

$$\frac{\partial \omega_k}{\partial \rho} = \frac{-3\omega_k + v_g k}{\rho}. \tag{A2}$$

The change in k and ρ result in a change in group velocity,

$$\delta v_g = \frac{\partial v_g}{\partial \rho}\delta\rho + \frac{\partial v_g}{\partial k}\delta k. \tag{A3}$$

Taking the derivative of Eq. (A2) with respect to k,

$$\frac{\partial v_g}{\partial \rho} = \frac{k - 2\mu v_g}{\mu\rho}, \tag{A4}$$

where $\mu = (\partial v_g/\partial k)^{-1}$ is the effective mass. Combining Eqs. (A1) and (A2) in Eq. (A3), and using Eq. (A4), we find

$$\delta v_g = \frac{1}{\rho}\left(\frac{3\omega_k}{\mu v_g} - 2v_g\right)\delta\rho. \tag{A5}$$

Now, from Eq. (3.7) the rate of change of ρ is proportional to the speed at which the lattice is transversed (here, we neglect η, which is assumed very small),

$$\dot{\rho}_n = \rho_n'\dot{n} \approx g\rho_n\dot{n} = gv_g. \tag{A6}$$

Thus, combining with Eq. (A5) the acceleration is

$$\dot{v}_g = \frac{dv_g}{d\rho}\dot{\rho} = \frac{gv_g}{\rho}\left(\frac{3\omega_k}{\mu v_g} - 2v_g\right). \tag{A7}$$

Since ω_k is a constant of motion, let us apply this result to the simplest case, that for which $\omega = 0$. Then we have

$$\dot{v}_g = -\frac{2g}{\rho}v_g^2. \tag{A8}$$

It is evident, as is intuitively clear, that since ρ is positive the acceleration is positive for negative g and vice versa. Now, to further understand this equation, let us integrate it, obtaining for the group velocity

$$\frac{1}{v_g(t)} = \frac{1}{v_g(0)} + 2g\int_0^t \frac{dt}{\rho(t)}. \tag{A9}$$

For $g > 0$ (i.e., the spacing grows as the wave packet advances) the integral in Eq. (A9) will converge as $t \to \infty$ to some value $1/w$ so the velocity will decrease until it converges to a finite final value,

$$\lim_{t\to\infty} v_g(t) = \frac{v_g(0)w}{v_g(0) + w} < v_g(0), \quad g > 0. \tag{A10}$$

Let us compare the result of Eq. (A9) with the quantal wave packet calculation of Fig. 8. Using the values $g = 0.001$, $v_g = 3.8$, and $\rho = 1$ in Eq. (A8), we find $\dot{v}_g = -0.03$ which is indeed the value seen in Fig. 8 as the initial acceleration after leaving the constant ρ zone (at about $T = 5$). While at short times Eq. (A8) is validated by the calculation, it is not validated at long times, where we do not see the velocity being stabilized. Our semiclassical analysis does not take into account the reflection (increased broadening) of the wave packet, which causes the expectation value to drop beyond the limit given in Eq. (A10).

Next, consider the case of $g < 0$. At short time, using the value $g = -0.001$ will give $\dot{v}_g = 0.03$ which is again verified by the quantal calculation shown in Fig. 8. At larger t the model predicts a catastrophic divergence: the velocity will grow and eventually diverge to infinity at a finite critical time t_c, for which the right hand side of Eq. (A9) vanishes. In the quantal calculation a similar behavior is indeed seen. It is seen as a rapid divergence of the velocity and acceleration as time proceeds. For example, at $g = 0.01$ (not shown in Fig. 8) the velocity grows from 3.8 to 15 within ten units of time.

[1] J. D. Joannopoulos, R. D. Meade, and J. N. Winn, *Photonic Crystals: Molding the Flow of Light* (Princeton University Press, Princeton, NJ, 1995).

[2] B. E. A. Saleh and M. C. Teich, *Fundamentals of Photonics* (Wiley, New York, 1991).

[3] K. C. Huang, P. Bienstman, J. D. Joannopoulos, K. A. Nelson, and S. Fan, Phys. Rev. B **68**, 075209 (2003).

[4] M. Quinten, A. Leitner, J. R. Krenn, and F. R. Aussenegg, Opt. Lett. **23**, 1331 (1998).

[5] S. A. Maier, P. G. Kik, H. A. Atwater, S. Meltzer, E. Harel, E. B. Koel, and A. A. G. Requicha, Nat. Mater. **2**, 229 (2003).

[6] S. A. Maier, P. G. Kik, and H. A. Atwater, Phys. Rev. B **67**, 205402 (2003).

[7] L. A. Sweatlock, S. A. Maier, H. A. Atwater, J. J. Penninkhof, and A. Polman, Phys. Rev. B **71**, 235408 (2005).

[8] A. M. van Oijen, M. Ketelaars, M. Matsushita, J. Kohler, T. J. Aartsma, and J. Schmidt, Biophys. J. **80**, 151a (2001).

[9] L. Markus, G. H. Christian, C. Thomas, E. Holger, B. Patrice, H. Andreas, M. Klaus, and B. Thomas, Phys. Rev. Lett. **92**, 103001 (2004).

[10] M. F. Garcia-Parajo, J. Hernando, G. S. Mosteiro, J. P. Hoogenboom, E. M. H. P. van Dijk, and N. F. van Hulst, ChemPhysChem **6**, 819 (2005).

[11] W. Rechberger, A. Hohenau, A. Leitner, J. R. Krenn, B. Lamprecht, and F. R. Aussenegg, Opt. Commun. **220**, 137 (2003).

[12] J. R. Krenn, J. C. Weeber, A. Dereux, E. Bourillot, J. P. Goudonnet, B. Schider, A. Leitner, F. R. Aussenegg, and C. Girard, Phys. Rev. B **60**, 5029 (1999).

[13] S. Maier, P. G. Kik, H. A. Atwater, S. Meltzer, A. A. G. Requicha, and B. E. Koel, Proc. SPIE **4810**, 12 (2002).

[14] S. A. Maier, P. G. Kik, and H. A. Atwater, Appl. Phys. Lett. **81**, 1714 (2002).

[15] M. L. Brongersma, J. W. Hartman, and H. A. Atwater, Phys. Rev. B **62**, 016356 (2000).

[16] L. Dobrzynski, A. Akjouj, B. Djafari-Rouhani, J. O. Vasseur, M. Bouazaoui, J. P. Vilcot, H. A. Wahsh, P. Zielinski, and J. P. Vigneron, Phys. Rev. E **69**, 035601 (2004).

[17] G. Christian, D. Erik, L. Mei, and M. Stephen, Phys. Rev. Lett. **97**, 100801 (2006).

[18] S. L. Westcott, J. B. Jackson, C. Radloff, and N. J. Halas, Phys. Rev. B **66**, 155431 (2002).

[19] K. Yabana and G. F. Bertsch, Z. Phys. D: At., Mol. Clusters **32**, 329 (1995).

[20] E. Prodan and P. Nordlander, Nano Lett. **3**, 543 (2003).

[21] R. Baer, S. Weiss, and D. Neuhauser, Nano Lett. **4**, 85 (2004).

[22] D. J. Sirbuly, M. Law, P. Pauzauskie, H. Q. Yan, A.V. Maslov, K. Knutsen, C. Z. Ning, R. J. Saykally, and P. D. Yang, Proc. Natl. Acad. Sci. U.S.A. **102**, 7800 (2005).

[23] M. Law, D. J. Sirbuly, J. C. Johnson, J. Goldberger, R. J. Saykally, and P. D. Yang, Science **305**, 1269 (2004).

[24] L. A. Sweatlock, S. A. Maier, H. A. Atwater, J. J. Penninkhof, and A. Polman, Phys. Rev. B **71**, 235408 (2005).

[25] J. C. Weeber, A. Dereux, C. Girard, G. C. des Francs, J. R. Krenn, and J. P. Goudonnet, Phys. Rev. E **62**, 7381 (2000).

[26] G. C. des Francs and C. Girard, Nanotechnology **12**, 75 (2001).

[27] A. Taflove and S. C. Hagness, *Computational Electrodynamics: The Finite-Difference Time-Domain Method* (Artech House, Boston, 2000).

[28] D. Neuhauser and R. Baer, J. Theor. Comput. Chem. **2**, 537 (2003).

[29] C. Girard and A. Dereux, Rep. Prog. Phys. **59**, 657 (1996).

[30] J. C. Weeber, A. Dereux, C. Girard, J. R. Krenn, and J. P. Goudonnet, Phys. Rev. B **60**, 9061 (1999).

[31] S. H. Chang, S. K. Gray, and G. C. Schatz, Opt. Express **13**, 3150 (2005).

[32] E. Runge and E. K. U. Gross, Phys. Rev. Lett. **52**, 997 (1984).

[33] R. Baer and D. Neuhasuer, J. Chem. Phys. **125**, 074709 (2006).

[34] S. A. Maier and H. A. Atwater, J. Appl. Phys. **98**, 011101 (2005).

[35] M. Sukharev and T. Seideman, J. Chem. Phys. **124**, 14707 (2006).

[36] U. Fano, Phys. Rev. **103**, 1202 (1956).

[37] J. A. Leegwater and S. Mukamel, Phys. Rev. A **46**, 452 (1992).

[38] R. Kosloff and D. Kosloff, J. Comput. Phys. **63**, 363 (1986).

[39] D. Neuhasuer and M. Baer, J. Chem. Phys. **90**, 4351 (1989).

[40] T. Seideman and W. H. Miller, J. Chem. Phys. **96**, 4412 (1992).